




Electrochemical energy storing performances of printed LaFeO₃ coated with PEDOT: PSS for hybrid supercapacitors

Reshma Nair^a, Kiranmai Uppuluri^b, Febin Paul^a, Keith Sirengo^c, Dorota Szwagierczak^b, Suresh C Pillai^c, Libu Manjakkal^{a,*} 

^a School of Computing and Engineering & the Built Environment, Edinburgh Napier University, Merchiston Campus, EH10 5DT, UK

^b Lukaszewicz Research Network, Institute of Microelectronics and Photonics, Kraków Division, ul. Zablocie 39, 30-701 Kraków, Poland

^c Nanotechnology and Bio-Engineering Research Group, Environmental Science, Faculty of Science, Atlantic Technological University, ATU Sligo, Ash Lane, Sligo F91YW50, Ireland

ARTICLE INFO

Keywords:

Hybrid supercapacitor
Screen printing
LaFeO₃
Perovskites
PEDOT: PSS
Graphite

ABSTRACT

Developing advanced smart energy storage devices demanded new functional materials to store energy effectively and deliver power quickly. In this work, we studied the energy-storing performance of perovskite material, lanthanum ferrite (LaFeO₃), prepared by the solid-state reaction method. The screen-printed LaFeO₃ and graphite electrodes are used to develop hybrid supercapacitors (HSCs) with KOH electrolyte. Varying the sintering temperature of the LaFeO₃ perovskite electrode (800 °C, 900 °C, and 1000 °C) leads to changes in the surface and crystalline properties, which impact the electrochemical properties and overall energy-storing performance of the HSC. The surface of the LaFeO₃ electrode is modified with organic conducting polymer poly(3,4-ethylenedioxythiophene) polystyrene sulfonate (PEDOT: PSS), which enhances the energy storage of the HSC. The developed HSC based on LaFeO₃, sintered at 1000 °C and surface modified with PEDOT: PSS, exhibited a specific capacitance of 12.007 mF•cm⁻² at a current density of 0.075 mA•cm⁻². This value is two times higher than (5.874 mF•cm⁻²) without the surface modification of LaFeO₃ at 1000 °C. This study provides valuable insights into the electrochemical performances of the ABO₃ perovskite (LaFeO₃) electrodes for the next generation of portable energy storage devices.

1. Introduction

In an era of advancements in artificial intelligence (AI), the electrification of vehicles and the rapid growth of portable electronics demanded efficient and sustainable energy storage systems for balancing energy management. Supercapacitors (SC), or ultracapacitors, have emerged as a key focus for researchers as an alternative to batteries due to their ability to charge and discharge rapidly without significant degradation [1–5]. They offer low-voltage applications and provide stable performance over a broad operating temperature range, high power density, long life cycle and utilisation of environmentally friendly materials for development [2–5]. Among the three major classifications of SCs such as (i) electrochemical double layer capacitor (EDLC), (ii) pseudocapacitor (PC), and (iii) hybrid supercapacitor (HSC), the HSC exhibited high performances as compared to EDLC and PC [6]. In HSC, two different types of electrodes were used as active electrodes in their fabrication [7]. The device's cathode uses a battery-type or

pseudocapacitive material to enhance energy density, while the anode employs EDLC materials for high power density. These systems combine the advantages of batteries—higher energy density—with the rapid power delivery capabilities of SCs [5]. For the fabrication of HSC, so far, various materials are employed and currently, researchers are focussed on the development of new sustainable materials for high-performing HSC fabrication [8].

ABO₃ perovskite materials, which are a type of ceramic, have gained significant attention in the field of energy storage due to their unique properties, including a cage-like structure that provides a high surface area, enabling a more significant number of active sites on the material's surface [2,3,9–14]. This, in turn, leads to high specific capacitance, enabling higher energy storage capacity. They also demonstrate high thermal and chemical stability and are compatible with various electrolytes, including aqueous and non-aqueous electrolytes, providing flexibility in design [15–17]. Furthermore, these materials are redox-active, cost-effective, and free from toxic elements, making them

* Corresponding author.

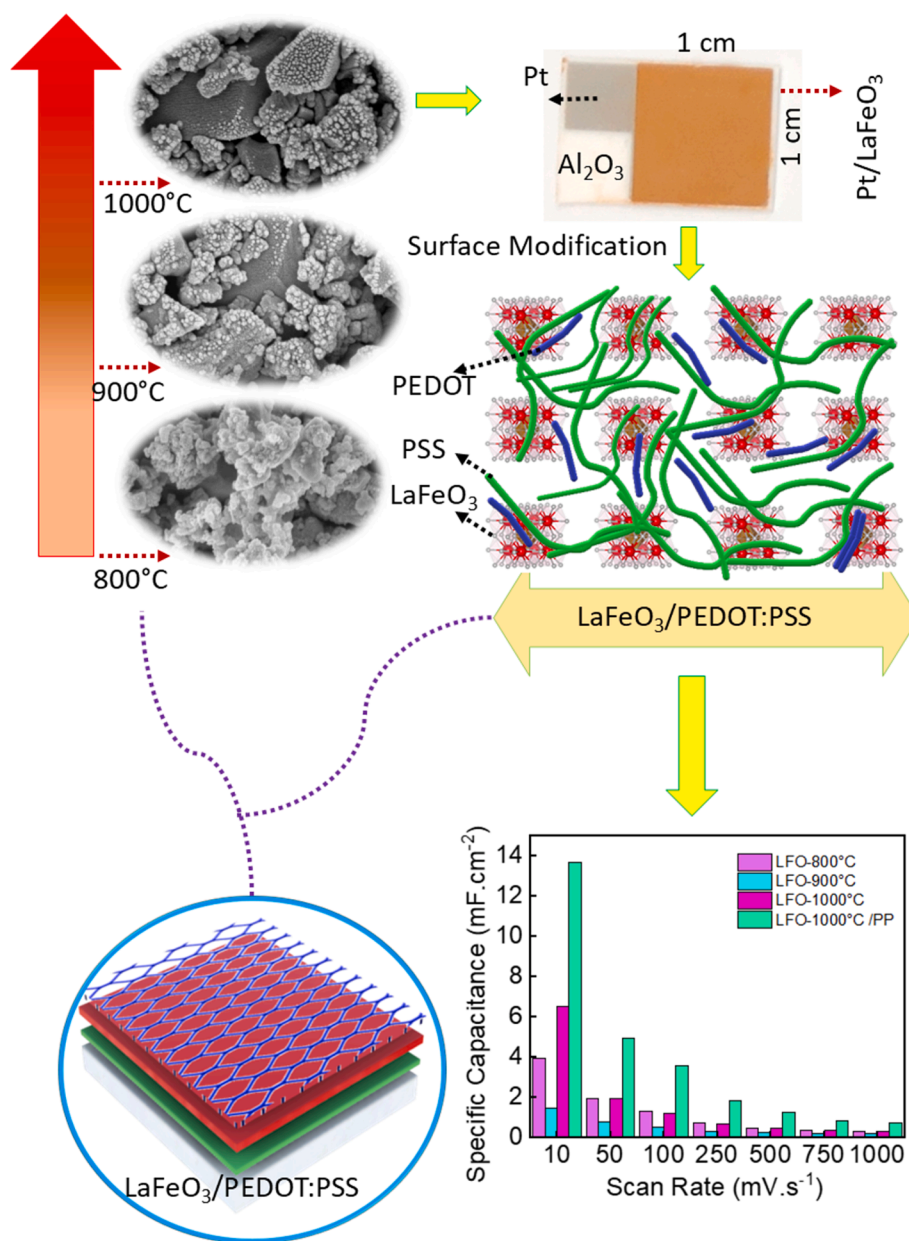
E-mail address: L.Manjakkal@napier.ac.uk (L. Manjakkal).

<https://doi.org/10.1016/j.cej.2024.158781>

Received 23 September 2024; Received in revised form 10 December 2024; Accepted 18 December 2024

Available online 20 December 2024

1385-8947/© 2024 The Author(s). Published by Elsevier B.V. This is an open access article under the CC BY license (<http://creativecommons.org/licenses/by/4.0/>).



Scheme 1. Outline of the research process.

sustainable [2–4]. These benefits, combined with high performance and fast charge/discharge rates, position ABO₃ perovskite materials as promising candidates for use in energy storage applications, particularly in developing high-performance and cost-effective SCs [9,16,18,19]. ABO₃ perovskite materials also have their disadvantages, such as semi-conductivity, environmental sensitivity, poor cyclic stability, and low energy density, impeding their broad implementation [11]. Despite these drawbacks, the recent recognition of LaFeO₃ as an effective perovskite electrode material for SCs is based on its excellent cycling stability, high discharge current, and capacity [11]. The significant advantage of LaFeO₃ in SC applications is its unique perovskite structure, which crystallizes in an orthorhombic arrangement that provides a high surface area and a more significant number of active sites for energy storage, resulting in high specific capacitance [20]. LaFeO₃ can be synthesized using cost-effective and scalable methods, including solid-state reactions, and its compatibility with various electrolytes (both aqueous and non-aqueous) allows for flexible design [21]. The material demonstrates high thermal and chemical stability, which is essential for

the longevity and reliability of SC. Furthermore, being cost-effective and free from toxic elements makes LaFeO₃ a sustainable option compared to traditional SC materials [22]. Overall, these factors position LaFeO₃ as a promising candidate for high-performance SCs.

In LaFeO₃, the rare earth elements lanthanum (La), iron (Fe), and oxygen (O) form the crystal structure, which consists of a three-dimensional network [15]. LaFeO₃ crystallizes in an orthorhombic perovskite structure, specifically within the Pnma space group [23]. In this arrangement, La³⁺ ions are coordinated by eight O²⁻ ions, while Fe³⁺ ions are octahedrally coordinated by six O²⁻ ions, resulting in corner-sharing FeO₆ octahedra, creating a cage-like structure [21]. However, the major downside of LaFeO₃ as an electrode material is its semi-conductivity, which hinders its ability to produce the desired results in practical applications. LaFeO₃ can conduct both ionic and electronic charge carriers, making it a mixed ionic-electronic conductor (MIEC) and a promising candidate for cathode applications [24,25]. LaFeO₃ allows for the accommodation of various cations and the creation of oxygen vacancies, which enables the material to exhibit both

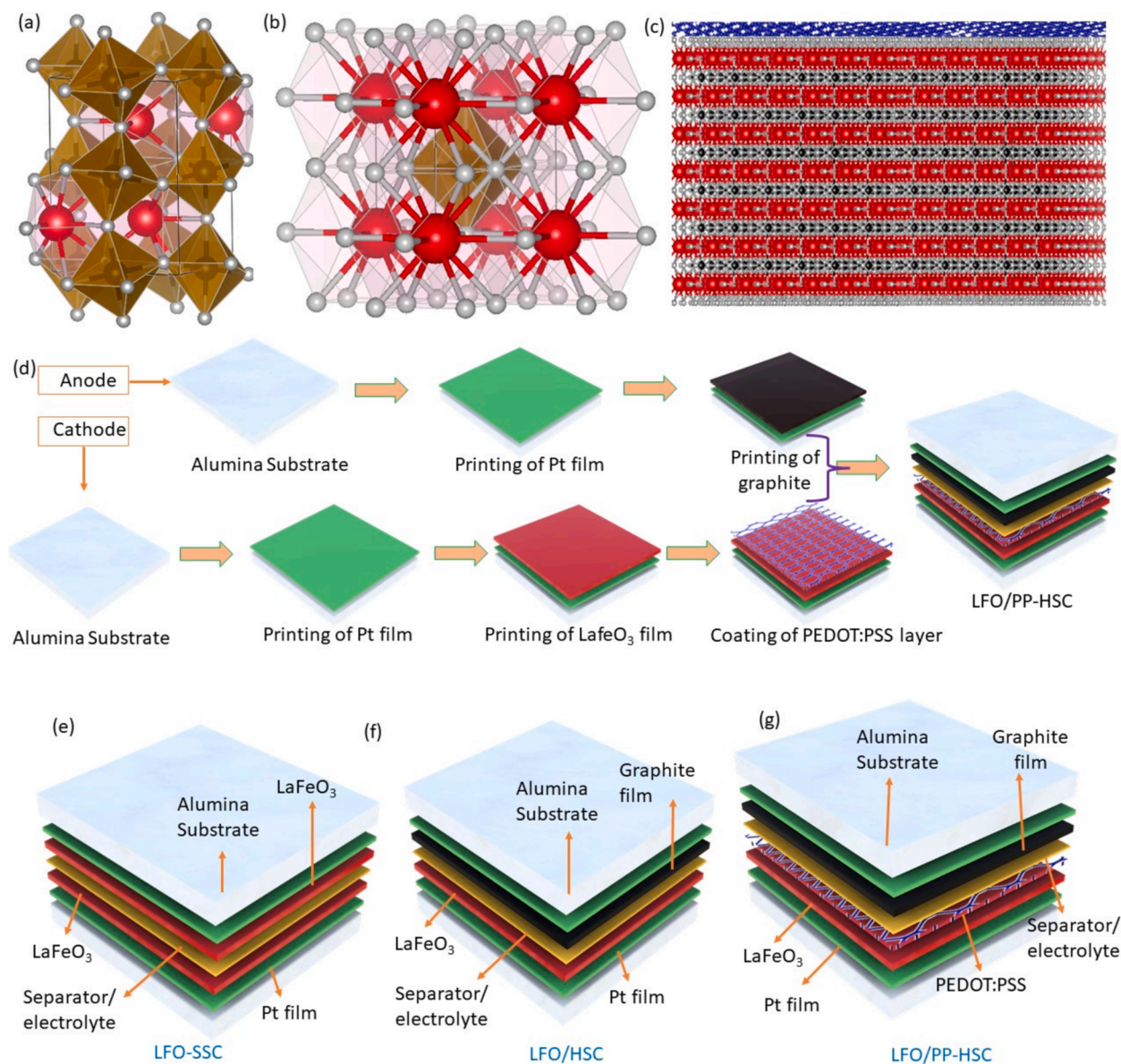


Fig. 1. (a) Crystalline structure of LaFeO_3 (b) Single-cell structure of LaFeO_3 (VESTA used for drawing) (c) Coating of PEDOT: PSS (blue colour) on the top of LaFeO_3 electrode (d) Fabrication steps of LFO/PP-HSC. (e) – (g) Schematic of LFO-SSC, LFO-HSC and LFO/PP-HSC.

ionic and electronic conduction [26]. The perovskite structure of LaFeO_3 allows for the creation of oxygen vacancies, which can facilitate the transport of O_2 through the crystal lattice. The mobility of these oxygen ions contributes to the ionic conduction in LaFeO_3 . As for electronic conduction, the presence of iron (Fe) in the LaFeO_3 structure can exist in multiple oxidation states (Fe^{3+} and Fe^{4+}) [20]. This variable oxidation state of iron allows for the hopping of electrons between the Fe^{3+} and Fe^{4+} sites, which enables electronic conduction in the material [27]. The ability to conduct both ions and electrons simultaneously allows LaFeO_3 to efficiently transport and exchange oxygen at the electrode–electrolyte interface, enhancing the overall performance and efficiency of these electrochemical devices [28]. LaFeO_3 can also be classified as a transition metal perovskite because of the presence of Fe and its multiple oxidation states ($\text{Fe}^{3+}/\text{Fe}^{2+}$), which are crucial for electron transfer properties in electrochemical and catalytic applications [29]. In addition to its redox activity, LaFeO_3 exhibits structural phase transitions in response to changes in temperature, pressure, and chemical composition, which substantially impact its electronic and magnetic properties [15]. The oxidation state of iron promotes conductivity and magnetic

behaviour and allows it to have tuneable semiconductor properties [29]. The rational choice of the components and fabrication methods, rational design, and attaining proper structural and morphological properties of electrode materials is crucial for progress in high-performance SC. In addition, the performance of SCs is heavily influenced by the structure, porosity, and morphology of electrode materials [30]. Given the semi-conductivity of pure LaFeO_3 , previous studies have reported modifications to its properties that enhance conductivity [11,20,22,31]. In one of the works, lanthanum ferrite with reduced graphene oxide ($\text{LaFeO}_3/\text{rGO}$) composite was prepared for SC development, showing cyclic stability for 3000 cycles [20]. The modifications of LaFeO_3 bulk properties, including its crystalline, morphology, and surface properties, will lead to addressing the conductivity and electrochemical limitations for optimizing the overall performance of SCs. In addition, utilization of such modified LaFeO_3 as an electrode of HSC offers several advantages by combining the benefits of an EDLC and pseudocapacitance mechanisms with the potential to revolutionise energy storage technology by improving energy density, power density and overall performance [5,32,33].

In this work, we studied the energy-storing performances of newly screen-printed LaFeO₃ perovskite for the next generation of HSC. The electrochemical and energy-storing performances of the LaFeO₃ were studied for the electrode prepared at different sintering temperatures and the electrode whose surface was modified using conductive polymer. We followed straightforward, inexpensive and effective methods of synthesis and deposition, such as the solid-state reaction of simple and stable oxides and screen printing, which led to the rational use of metals (in our case, La, Fe, Pt). Scheme 1 represents the research process along with the image of the printed LaFeO₃ electrode. The detailed energy-storing performances of the LaFeO₃ were fine-tuned by varying the crystalline and surface morphology by changing the sintering temperature (800 °C–1000 °C) while preparing the LaFeO₃ electrode. The surface modification of the perovskite electrodes was carried out by reacting with an organic conducting polymer poly (3,4-ethylene dioxithiophene) polystyrene sulfonate (PEDOT: PSS). Here, the conductive polymer acts as an interlinked conductive layered network, as shown in the scheme. The PEDOT: PSS enhances energy storage performance through the formation of an EDLC and pseudocapacitance resulting from the reaction of conjugated polymers. Based on these electrodes, we developed two sets of HSCs and a symmetric supercapacitor (SSC), which consists of set 1 based on LaFeO₃ (LFO-SSC), set 2 based on pristine LaFeO₃ (LFO-HSC) and set 3 based on the LaFeO₃/PEDOT: PSS (LFO/PP-HSC). We found that LFO/PP-based electrodes, in which the LaFeO₃ layer was sintered at 1000 °C coated with PEDOT: PSS, exhibit high performances (12.007 mF•cm⁻² at a current density of 0.075 mA•cm⁻² as shown in the scheme) due to their crystalline structure, porous surface morphology, high conductivity, and contribution of both EDLC and pseudocapacitance.

Fig. 1a illustrates the crystalline orthorhombic structure of LaFeO₃ perovskite. In contrast, Fig. 1b displays a single unit of the LaFeO₃ structure where black, red, and white spheres denote Fe, La, and O atoms, respectively. Fig. 1c shows the conductive layered network of PEDOT: PSS with LaFeO₃. Here, for the HSC development, the LaFeO₃ acts as a cathode electrode, and graphite acts as an anode electrode. The fabrication steps of LFO/PP-HSC are shown in Fig. 1d. The schematics of Fig. 1e, 1f and 1g show the comparison of LFO-SSC, LFO-HSC and LFO/PP-HS. Here, the performances of standalone LaFeO₃ are discussed via the fabrication of SSC, and the inclusion of graphite electrodes in HSC enhances the overall performance and stability of the SC [34]. SCs are constructed using an electrolyte of 6 M KOH (potassium hydroxide) and a polyester/cellulose blend separator (Techni Cloth, TX 612) [21,35–37]. The research introduces an approach by utilizing a pure LaFeO₃-based electrode, which was drop-casted with a conducting polymer, PEDOT: PSS. This method aimed to enhance the electrode's conductivity, leading to improvements in specific capacitance, energy density, and cyclic stability. These enhancements have promising implications for applying such electrode materials in electrochemical energy storage devices.

2. Experimental Section/Methods

2.1. Materials and electrode fabrication

LaFeO₃ was synthesized using the solid-state reaction method. Starting oxides La₂O₃ (99.9 %, Sigma-Aldrich) and Fe₂O₃ (99.8 %, Sigma-Aldrich) were mixed in stoichiometric proportions (1:1 M ratio) and milled for 8 h in isopropyl alcohol using a ball mill (Pulverisette 5, Fritsch, Germany), agate containers and agate balls. The powder, after drying, was pressed into pellets, which subsequently were calcined at 1200 °C for 20 h to perform the synthesis. The major advantages of pelletizing and heating the product rather than treating it in powdered form are (i) pelletizing facilitates easier handling and reduces material waste, and (ii) pelletized material allows for a more compact arrangement of grains of the oxides involved. Pressing the mixed oxide reagents into pellets increases the contact surface area between the grains of two

reacting oxides, facilitates diffusion in the solid state, and consequently increases the effectiveness of the solid-state synthesis reaction. Applying properly synthesized single-phase, pure perovskite material in the functional layer is crucial for the resulting material properties and device performance. The synthesized product was ball-milled for 8 h and used to prepare a thick film paste. The oxide powder was manually mixed in an agate mortar with a binder (ethyl cellulose) and solvent (terpineol).

In this work, both SSC and HSCs were developed, and for this, the active electrodes LaFeO₃ and graphite were printed using screen printing (image of the printed electrode shown in Fig. S1). For LaFeO₃-based electrode fabrication, the Al₂O₃ substrates (96 %, Kyocera) with dimensions 10 x 15 mm were covered with conductive thick film from Pt-based ESL 5542 paste using a screen-printing method and fired at 1000 °C for 15 min (Fig. 1d). Pt serves as current collector in this system which is used for the efficient charge transfer between the electrodes and the external circuit with minimized energy losses. Pt is a commonly used current collector material known for its high electrical conductivity, structural integrity, and chemical and thermal stability. Then, the prepared LaFeO₃ – based paste was screen printed on the previously fired Pt-based thick film and sintered for 1 hr at 3 different temperatures: 800, 900 and 1000 °C. The surface area of the printed LaFeO₃ films was precisely established at the step of designing masks for screen printing patterns. The shrinkage of the layer at a level 15–20 % could be determined based on heating microscope studies and using a digital optical microscope (Fig. S2). Hence, the developed SC electrode size is 1 cm x 1.5 cm, with an actual active area of the electrode of 1 cm² (Fig. S1). For the hybrid SC, the graphite electrode acts as the anode, and for the fabrication of this electrode, carbon-polymer paste (DuPont 7102) was screen printed on the top of the conductive Pt-based layer and subsequently cured at 130 °C for 30 min. The steps of fabrication of graphite and LaFeO₃ electrodes are given in Fig. 1d. To enhance the performance of LaFeO₃, the conductive polymer was coated on the top of the electrode. For this, the PEDOT: PSS (Ossila M122-1000 ml) and 5 wt% dimethyl sulfoxide (Sigma-Aldrich) were used to prepare the drop-casting solution by carefully blending them using a magnetic stirrer for 15 min. A volume of 5 μL was drop-casted using a pipette and allowed to spread, forming a thin coated layer over the active material LaFeO₃ through surface tension and the force of gravity. After forming a thin layer, it was dried in an oven for 1 hr at 80 °C and repeated twice.

2.2. Device fabrication

The screen-printed electrodes were connected to external wires by soldering them onto the current collector (Pt layer). Insulation paste (TPU Protection Ink – JE Solution) was applied to prevent short circuits, and the electrodes were dried in an electric oven for 15 min at 80 °C. A polyester/cellulose blend separator (Techni Cloth, TX 612) and an aqueous liquid-based 6 M KOH (Sigma-Aldrich) solution were used as the electrolyte. The separator is placed between the electrodes to separate the active area, thereby preventing potential short circuits. Before device assembly, the separator should be wetted in the electrolyte for 15 min to facilitate electrolytic absorption, ensuring optimal performance. The high concentration of KOH increases ionic conductivity in electrolytes, enhancing charge transfer processes, which is effective for LaFeO₃'s performance as an electrode material. The wetted separator was placed on top of one of the electrodes using tweezers. Subsequently, the second electrode was positioned on top of the separator to ensure complete separation of the electrodes. This configuration forms a sandwich-like structure, creating an electrode–electrolyte–separator–electrolyte–electrode stack shown in Fig. 1d. Based on the printed electrodes, we developed two sets of HSCs and an SSC, which consist of set 1 based on LaFeO₃ (LFO-SSC), set 2 based on pristine LaFeO₃ (LFO-HSC), and set 3 based on the LaFeO₃/PEDOT: PSS (LFO/PP-HSC) represented in Fig. 1e–1g. The same printed LaFeO₃ electrodes were used for an SSC arrangement, while for HSC, printed LaFeO₃ and graphite

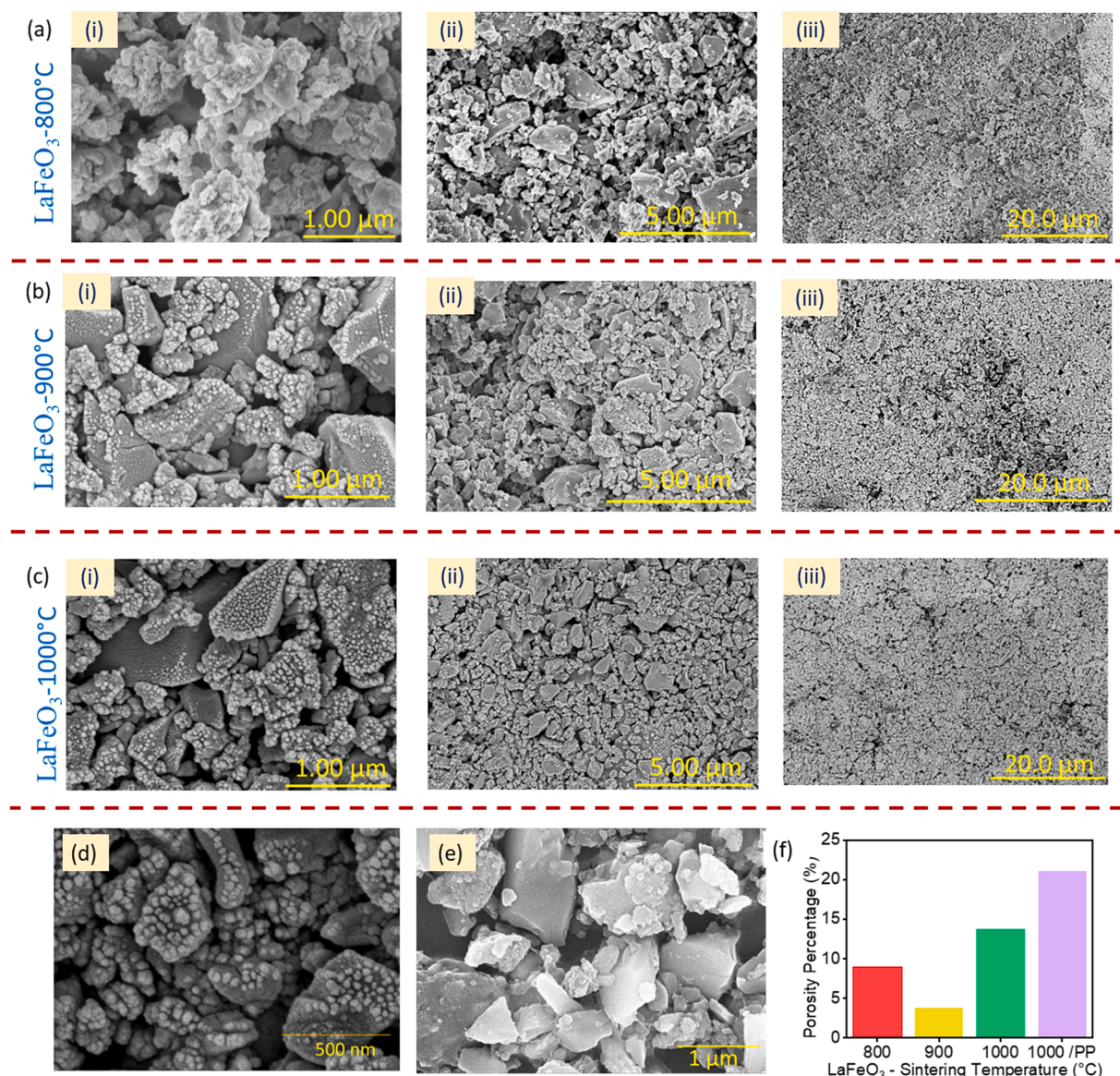


Fig. 2. SEM images screen printed (a) LaFeO₃ – 800 °C (b) LaFeO₃ – 900 °C (c) LaFeO₃ – 1000 °C (d) LaFeO₃ – 1000 °C, 500 nm (e) LaFeO₃ – 1000 °C/PEDOT: PSS (f) Porosity percentage of LaFeO₃ samples.

electrodes were sandwiched together. Finally, the entire SC stack was encapsulated with encapsulation material (PVC cling film) to protect the electrolyte leakage, electrodes, and separator from moisture and mechanical damage.

2.3. Material characterisation

Morphological analysis was conducted using Scanning Electron Microscopy (SEM) with a Hitachi S-4800 Cold Field Emission High-Resolution Scanning Electron Microscope, conductive material coating used is palladium (Pd) metal. ImageJ software was used for porosity calculation from SEM images [38]. The elemental composition and crystallization were investigated using Energy Dispersive X-ray Spectroscopy (EDX) with an Oxford Instruments Inca X-act system connected to the Hitachi S-4800 SEM. Contact angle measurements were performed using an Ossila contact angle goniometer. X-Ray- Diffractometer (XRD, Bruker D8 Advnace Eco) was used to analyse the composition crystal structure (ref. code: 98–015-3536, ICSD code: 153536). Fourier Transform Infrared Spectroscopy (FTIR) was conducted using a Perkin Elmer Frontier FTIR machine, capable of mid-IR (8300–350 cm⁻¹) and

far-IR (700–30 cm⁻¹) analysis, with a maximum resolution of 0.4 cm⁻¹.

2.4. Electrochemical characterisation

The electrochemical experiments were conducted using a two-electrode configuration, where the measured voltage is the device voltage in this setup. The electrochemical characterization Cyclic Voltammetry (CV), Electrochemical Impedance Spectroscopy (EIS), and Galvanostatic charge–discharge (GCD) was carried out using the electrochemical workstation (IviumStat.h). The CVs were carried out at different scan rates between 1 mV•s⁻¹ to 2000 mV•s⁻¹. The EIS was taken from lower frequencies (1 MHz and 10 Hz) to a higher frequency (1 MHz). The GCD was carried out at various current densities respective to the device at 1 V for HSCs and at 0.8 V for SSCs. HSCs generally have higher voltage limits than traditional SCs, but the voltage limit for cells with liquid electrolytes is constrained by the electrolysis of water, which has a theoretical limit of 1.23 V at room temperature. Aqueous electrolytes in HSCs can often operate slightly above this limit due to overpotential effects, while the voltage range for SSCs is generally lower than that of HSCs.

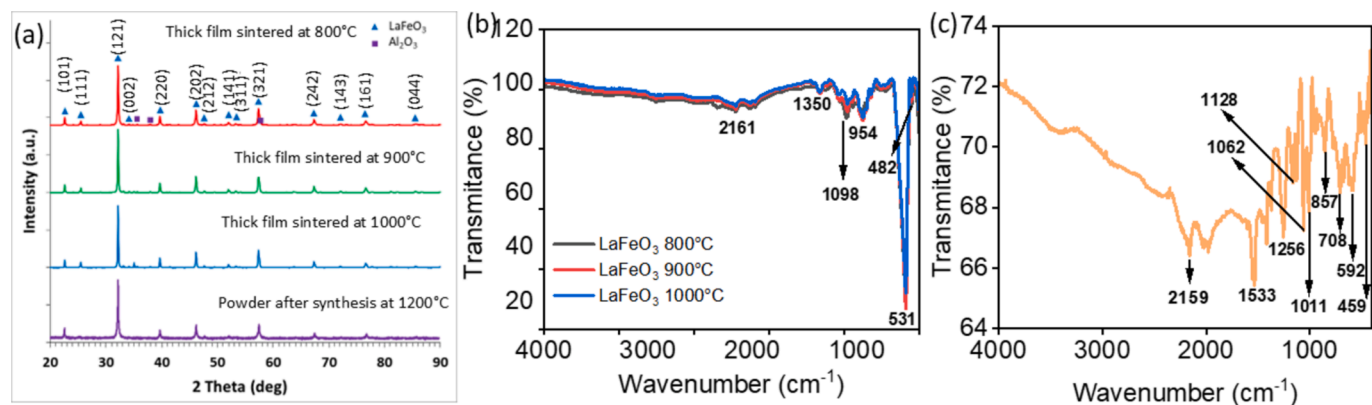


Fig. 3. (a) XRD of LaFeO₃ for 800 °C, 900 °C, 1000 °C and LaFeO₃ powder after synthesis at 1200 °C (b) FTIR of LaFeO₃ 800 °C, 900 °C, 1000 °C (b) FTIR of LaFeO₃ with PEDOT:PSS.

The SC's performances were calculated using CV and GCD techniques [39–41]. The following equation can be used to compute the capacitance from CV:

$$C_{CV} = \frac{1}{2vA\Delta V} \int Idv$$

Where, I is the response of Current (A), V is the potential (V), v is the Scan Rate ($V \cdot s^{-1}$), A is the area of active material (cm^2), ΔV is the potential range (V). Capacitance is calculated using GCD as follows:

$$C_{GCD} = \frac{I \Delta t}{A \Delta V}$$

Where, I is the applied constant current (A), Δt is the discharge time (s), A is the area of active material (m or cm^{-2}), and ΔV is the discharge Voltage (V). Energy density in charged SCs is influenced by the capacitance of the device and the operating cell voltage. The ED can be computed using the GCD curve as follows:

$$E = \frac{1}{2} C(\Delta V)^2$$

Where C is the total Capacitance (F) and ΔV is discharge Voltage (V). Power density is the rate at which the charge is sent to an external source. The power density can be computed using the GCD curve as follows:

$$P = \frac{E}{\Delta t}$$

Where E is the energy density, and Δt is the discharge time.

3. Results and Discussion

3.1. Morphological and structural analysis

The SEM image of the LaFeO₃ sintered at 800 °C, 900 °C and 1000 °C are shown in Fig. 2a to 2c, revealing notable structural changes. The SEM reveals a rough uniform distribution of crystalline LaFeO₃ particles. In low magnification (1 μm), LaFeO₃ appears as a cluster of particles of varying sizes, with discernible grain boundaries and agglomerated particles. Further examination at higher magnifications (5 and 20 μm) shows the presence of individual grains, which are more distinct, exhibiting rectangular shapes with rough surfaces, and small pores are visible both within the grains and between them. The findings suggest that the sintering temperature substantially influences the surface morphology of the material. For electrochemical energy storage, the microstructural properties, porosity and electrical conductivity are some of the critical factors influencing the performance. It was noticed, at 800 °C, incomplete sintering leads to higher porosity and suboptimal grain connectivity. However, the finer grains result in a larger surface area, and it will be supportive for electrochemical performance. However, sintering at 1000 °C results in a well-sintered material with higher porosity and improved grain connectivity, optimizing both conductivity

and overall performance. This is supported by the SEM images at 1 μm of LaFeO₃ samples sintered at different temperatures, as shown in Fig. 2a (i), 2b(i) and 2c(i). Phase purity is another crucial aspect, with grain boundary effects further influencing performances. The 800 °C sample may contain some impurity phases, while the 1000 °C sample exhibits high phase purity, thereby enhancing its intrinsic properties. This is evident from Fig. 2d, which shows the SEM images of the LaFeO₃ 1000 °C sample taken in the 500 nm range. The 900 °C sample may suffer from unwanted secondary phases due to incomplete phase formation. Smaller grains in the 800 °C sample increase capacitance, while the larger grains in the 1000 °C sample reduce grain boundary resistance, thereby improving charge transfer. The 900 °C sample may exhibit suboptimal grain boundary characteristics [42]. Interfacial properties with graphite are also vital. The 800 °C sample maintains reasonable interfacial contact, while the 1000 °C sample achieves optimal contact, enhancing charge transfer. In contrast, the 900 °C sample may have less effective interfacial properties due to thermal stresses.

In the case of the LaFeO₃ –1000 °C electrode drop-casted with PEDOT: PSS, resulting in the formation of small pores on the electrode surface as given in Fig. 2e and Fig. S3a and S3b in supporting information. The SEM imaging confirms that solvent evaporation results in porosity on the electrode surface, and the pores in the thin layer reveal the LaFeO₃ particles. The SEM images provide a clear view of the crystal formation through the pores, confirming the distinctive rectangular structure identified as the structure of the LaFeO₃ particles. The presence of porosity within the electrode structure also contributes to higher efficiency, and the calculated porosity percentages are presented in Fig. 2f. In addition to this, from the SEM image depicted in Fig. S3c, it becomes evident that the screen-printed graphite electrode exhibits a homogeneous dispersion of the active material. The electrode's surface is not uniformly smooth, exhibiting discernible irregularities, eventually increasing the surface area and leading to high performance. The porosity within the graphite electrode structure also contributes to higher efficiency. We also performed the SEM analysis for a sample sintered at 700 °C and 1100 °C, and the images are provided in Fig. S4 in supporting information.

The EDX analysis for LaFeO₃ 1000 °C confirms the presence of lanthanum (La), iron (Fe), and oxygen (O) in the material, with weight percentages of 52.7 %, 21.2 %, and 18.8 %, respectively, and atomic percentages of 19.2 %, 19.2 %, and 59.68 %, respectively shown in Fig. S5a. The remaining weight percentage of 7.1 % and atomic percentage of 1.85 % are attributed to the current collector, Pt. Further, we also measured the EDX of LaFeO₃ 1000 °C /PEDOT: PSS. The EDX analysis identified the presence of La, Fe, O, S, and Na, with weight percentages of 25.16 %, 10.73 %, 32.40 %, 22.87 %, and 2.27 %, and atomic percentages of 5.58 %, 5.92 %, 62.43 %, 21.99 %, and 3.04 %, respectively.

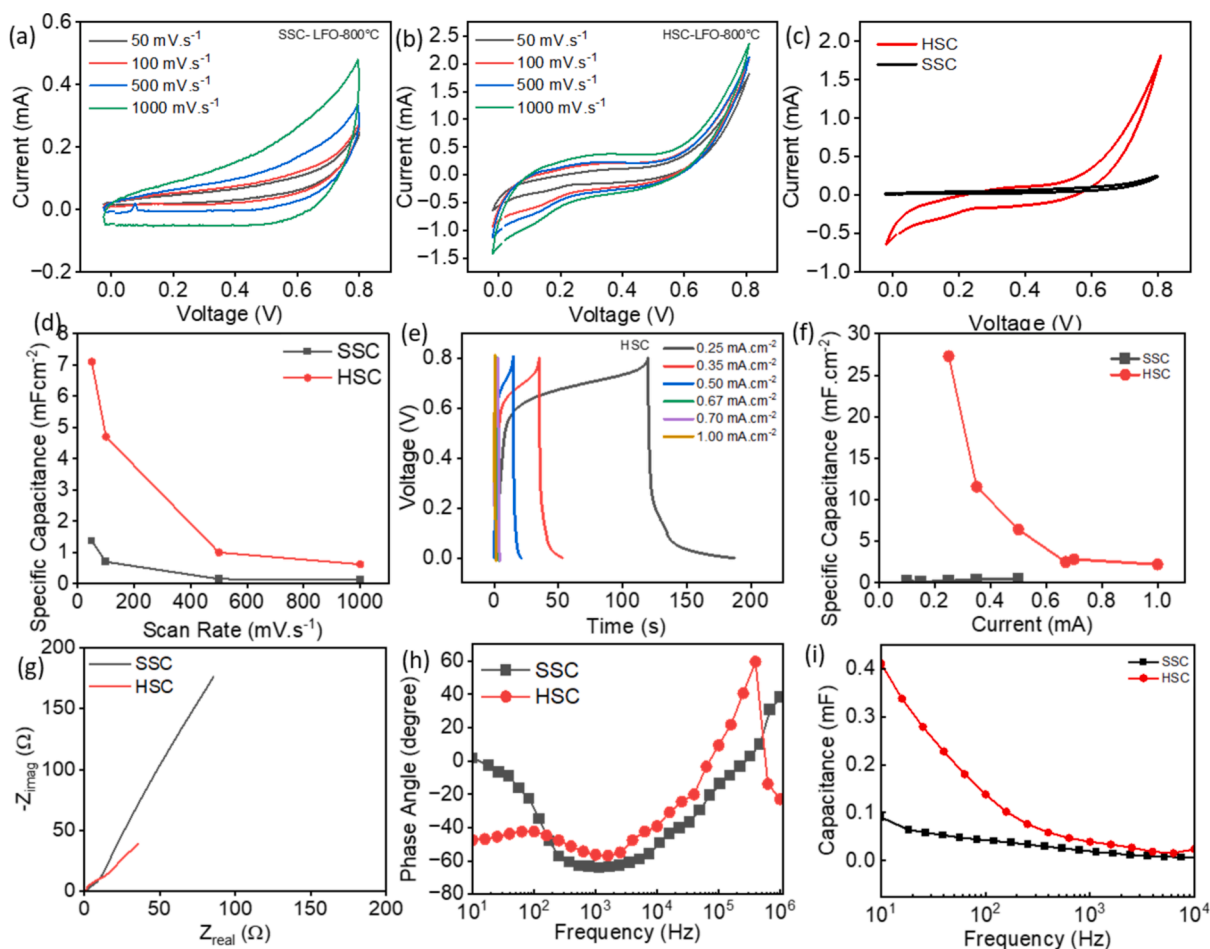


Fig. 4. CV curves of (a) SSC (b) HSC (c) Comparison $50 \text{ mV}\cdot\text{s}^{-1}$ of HSC and SSC at 0.8 V (d) Specific Capacitance from CV curve (e) GCD curves of HSC at different scan rates (f) Specific Capacitance from GCD curve (g) Nyquist plot (h) Bode plot (i) Capacitance from EIS data.

respectively, at the specific spot (Fig. S5b). The remaining weight percentage of 6.57 % and atomic percentage of 1.04 % are attributed to Pt, the current collector.

The contact angle measurements of LaFeO_3 - 800°C , LaFeO_3 - 900°C , LaFeO_3 - 1000°C , LaFeO_3 - 1000°C /PEDOT: PSS and graphite are shown in Fig. S6 (a) to S6 (e) for the 6 M KOH electrolyte, and the angle is observed as 12° , 15.86° , 18° , 51° , & 108° , respectively indicating a robust surface interaction. This can be attributed to the highly hydrophilic nature of the LaFeO_3 surface, which facilitates favourable interaction with the electrolyte. After coating the LaFeO_3 with PEDOT: PSS, the contact angle increased to 51.18° from 18° , suggesting that the electrolyte is still suitable for further studies that utilize hydrophobic electrolyte systems despite being below 90° [43]. This change in contact angle indicates that the super hydrophilic nature of the LaFeO_3 surface was primarily replaced by the hydrophobic PEDOT: PSS coating. Although PEDOT: PSS is typically hydrophobic to KOH, the presence of LaFeO_3 in the underlying coating alters its properties. This suggests that the drying solvent creates small pores that allow the electrode to act as a double layer of PEDOT: PSS and LaFeO_3 . The combination of the highly hydrophilic LaFeO_3 material and the hydrophobic PEDOT: PSS coating results in an intermediate contact angle, which is still suitable for the electrolyte system used in the study. The formation of small pores during drying further enhances the interaction between the electrode and the electrolyte.

The X-Ray-Diffractometer (XRD) method was used for the analysis of the phase composition of the synthesized powder and LaFeO_3 thick films sintered at 800°C , 900°C and 1000°C . Fig. 3a compares XRD patterns of thick films sintered at various temperatures (800 , 900 and 1000°C)

and the LaFeO_3 powder after synthesis at 1200°C for comparison. The Lanthanum ferrite (III) LaFeO_3 phase, which crystallizes in the orthorhombic system, space group Pnma, was detected in all samples, independently of the sintering temperature. Small amounts of Al_2O_3 crystalline phase originating from the substrate were identified for the thick films screen printed and fired on alumina. In addition to the above studies, a detailed structural analysis of the samples sintered at 700°C and 1100°C was also carried out. It was found that neither lowering the sintering temperature to 700°C nor increasing it to 1100°C causes a significant change in the phase composition of LaFeO_3 thick films. The film sintered at 700°C was not well sintered in contrast with that sintered at 1100°C . This was confirmed by observations using a heating microscope (Fig. S2), which revealed that a distinct shrinking of the sample started above 900°C . Comparison of the XRD pattern for the films sintered at 700 - 1100°C was shown in Fig. S7.

Fig. 3b shows the FTIR analysis of screen-printed LaFeO_3 electrodes sintered in different temperatures (800°C , 900°C , 1000°C) in the frequency range of 4000 to 400 cm^{-1} . The FTIR analysis of LaFeO_3 - 800°C identified a total of 6 peaks in the spectrum. The peak observed in the range of 400 cm^{-1} to 600 cm^{-1} is attributed to the bending and stretching vibrations of the Metal-Oxygen (M-O) bond, specifically the B-O bond in the ABO_3 perovskite structure, which is Fe-O in this sample. [44]. The peaks at 482 cm^{-1} and 531 cm^{-1} indicate a well-organized material arrangement and the structural stability of the LaFeO_3 system. The absorptions in the fingerprint region (400 cm^{-1} - 500 cm^{-1}) are comparable to the asymmetric stretching and bending vibrations of O-M-O and M-O-M [22]. The M-O stretching vibrations can be detected in the range of 500 cm^{-1} to 600 cm^{-1} . The peaks at 482 cm^{-1}

are associated with the O-Fe-O vibrations of the LaFeO_3 compound [45]. The significant vibration of the octahedral FeO_6 group in LaFeO_3 is the Fe-O stretching vibration, which is responsible for the peaks at 531 cm^{-1} in the spectra. The pure LaFeO_3 's IR peak at 954 cm^{-1} is attributed to the symmetric stretching vibration of the carbonate, while the peak at around 1350 cm^{-1} is due to the asymmetric stretching vibration of the carboxyl group [46–48]. The increasing temperature leads to similar peaks with more intensive transmittance data.

Fig. 3c shows that the FTIR spectrum of the LaFeO_3 -1000 °C/PEDOT:PSS electrode exhibits a total of 11 peaks in the same frequency range. The peak at 1533.18 cm^{-1} can be attributed to the C = C stretching vibration of the thiophene ring in PEDOT, a typical peak observed in the FTIR spectra of PEDOT:PSS and its derivatives [49]. The peak at 1256.72 cm^{-1} can be attributed to the C-O stretching vibration of the ester group in PEDOT:PSS, suggesting the presence of chemical bonding between LaFeO_3 /PEDOT:PSS, which might involve changes in the conformation of the polymer chains or interactions with the LaFeO_3 . The peak at 1164.55 cm^{-1} can potentially be attributed to the C-O stretching vibration in PEDOT:PSS or the metal–oxygen vibration in LaFeO_3 , as perovskite materials like LaFeO_3 often exhibit metal–oxygen vibrations in the $400\text{--}800\text{ cm}^{-1}$ range. The peak at 1128.84 cm^{-1} can be attributed to the C-O stretching vibration of the PEDOT:PSS layer. The FTIR spectrum also shows a peak at 1062.09 cm^{-1} , which could be attributed to the stretching vibration of the S-O bond in the PEDOT:PSS coating, as this is a typical peak observed in the FTIR spectra of PEDOT:PSS and is typically found around the $1040\text{--}1070\text{ cm}^{-1}$ range. Alternatively, the peak at 1011.49 cm^{-1} could be due to the stretching vibration of the S = O bond in the PEDOT:PSS layer, but this assignment is less likely as the S = O stretching band is typically weaker and appears at a slightly higher wavenumber, around $1030\text{--}1050\text{ cm}^{-1}$ [50]. The peak at 857.42 cm^{-1} can be of the C-H bending vibration of the PEDOT:PSS component. The peak at 708.14 cm^{-1} can potentially be attributed to the Fe-O stretching vibration, which is typically observed in the range of $500\text{--}700\text{ cm}^{-1}$ for iron oxides. The peak at 592.89 cm^{-1} can be attributed to the Fe-O stretching vibration, which is a common vibration observed in LaFeO_3 , or the C-S stretching vibration in PEDOT:PSS. The last peak at 459.27 cm^{-1} can potentially be attributed to the metal–oxygen vibrations in the LaFeO_3 material. [51]. The inclusion of PEDOT:PSS in the LaFeO_3 electrode has introduced additional peaks in the FTIR spectrum, which can be attributed to the characteristic vibrations of the PEDOT:PSS polymer. A significant observation is the disappearance of the strong absorption band corresponding to the metal–oxygen bonds in the modified electrode. This finding suggests that the electrode modified with PEDOT:PSS exhibits enhanced conductivity and an increased presence of organic compounds. The absence of the metal–oxygen peak indicates that the PEDOT:PSS coating alters the chemical environment at the electrode surface, potentially leading to improved electrode performance. The enhanced conductivity provided by the PEDOT:PSS layer facilitates efficient charge transport within the electrode material. The presence of additional organic compounds originating from the PEDOT:PSS coating likely contributes to the improved electrode performance.

3.2. Electrochemical characterization

Electrochemical properties of SSC and HSC: Prior to characterizing the electrochemical performances of HSC, an initial analysis was carried out for the SSC device. Here the device SSC is symmetrically designed, with its anode and cathode composed of screen-printed pure LaFeO_3 (sintered at 800 °C). While analysing the CV curves of the SSC, we observed that, the development of pseudo capacitance with a half-quasi-rectangular shape as shown in Fig. 4a. However, there are no exact mirror image current responses, and the reduction peak is nearly at the baseline, accompanied by fluctuations resembling noise. This suggests that the device lacks high capacitance or energy density, possibly due to the poor formation of a surface reaction on the device [52,53]. This is further compounded by the fact that pure LaFeO_3 is semi-conductive.

This contributes to poor CV performance, but half quasi-rectangular shape showcases that the LaFeO_3 has considerable potential for good pseudo-capacitive performance, higher stability, and sustainable behaviour [54,55]. Further to this, the CV curves of the HSC device (here LaFeO_3 sintered at 800 °C) are shown in Fig. 4b. The CV of HSC shows stability and a large area under the scan voltage range, which means higher specific capacitance compared to SSC. To compare the performance of HSC and SSC, Fig. 4c presents the CV response of both devices at a scan rate of $50\text{ mV}\cdot\text{s}^{-1}$ at 0.8 V . Upon analyzing these curves, it becomes evident that HSC shows an excellent CV response, with nearly symmetrical current profiles during both oxidation and reduction processes. Furthermore, HSC displays a larger polynomial area covering oxidation and reduction processes, indicating superior capacitive performance and SSC exhibits a poor polynomial area with a nearly flat curve. The specific capacitance of HSC, measured at this scan rate is $7.1\text{ mF}\cdot\text{cm}^{-2}$, which is 5 times higher compared to SSC, which has a specific capacitance of $1.37\text{ mF}\cdot\text{cm}^{-2}$. When we calculate the specific capacitance and peak current in Fig. 4d and Fig. S8a respectively, it's clear that HSC has good characteristics in terms of this specific capacitance compared to SSC. Additionally, the maximum peak current values for HSC (Fig. S8a) reach a higher peak of 2.37 mA , which is significantly greater than the peak current of 0.48 mA observed for SSC at a scan rate of $1000\text{ mV}\cdot\text{s}^{-1}$. This supports the HSC's ability to efficiently store and release charge. Furthermore, the stability of CV curves of HSC is noteworthy, oxidation and reduction curves are stable which suggests that the device's performance remains consistent over time. This means the device HSC is overall stable and reliable.

The GCD curves of HSC and SSC in different current densities are demonstrated in Fig. 4e and Fig. S8b, respectively. The comparison of GCD curves for HSC and SSC at a current density of $0.25\text{ mA}\cdot\text{cm}^{-2}$ reveals specific capacitance values of $0.25\text{ mF}\cdot\text{cm}^{-2}$ for SSC and $27.28\text{ mF}\cdot\text{cm}^{-2}$ for HSC, indicating that the specific capacitance of HSC is almost 100 times larger than that of SSC, as shown in Fig. S8c. The GCD curves of SSC have higher voltage drops and poor reversibility compared to HSC, which is reflected in the capacitive contribution presented in Fig. 4f. Sudden discharge can be found in SSC, it can be due to the internal resistance of the device SSC. The internal resistance may lead to poor performance and cause more heat while charging and discharging [56]. The energy density and power density of both HSC and SSC were measured and plotted in Fig. S8d. The highest energy density for HSC is $1.4284\text{ }\mu\text{Whcm}^{-2}$, while for SSC, it is significantly lower at $0.01223\text{ }\mu\text{Whcm}^{-2}$. In terms of power density, HSC achieves $76.75\text{ }\mu\text{Wcm}^{-2}$ compared to SSC's $31.45\text{ }\mu\text{Wcm}^{-2}$. It can be concluded that the current density is inversely proportional to the capacitance and energy density and directly proportional to the power density [57].

The electrochemical impedance spectroscopic (EIS) measurements were carried out within the frequency range of 10 Hz to 1 MHz . Fig. 4g and 4 h present the Nyquist and Bode plots resulting from the EIS, respectively. In the high-frequency region of the Nyquist plot, the equivalent series resistance (ESR) was determined to be $0.12\text{ }\Omega$ for SSC and $0.03\text{ }\Omega$ for HSC. Upon analyzing the Nyquist plot, it is noted that SSC demonstrates relatively high impedance, in the higher frequency range, suggesting that the electrodes hinder the effective movement of ions through the pore structures. In EIS, the ESR refers to the impedance resulting from the resistance of the electrolyte and the flow of current through it. In HSC, a small visible semi-circle formation in this plot suggests the presence of charge transfer resistance and the inclined line at 45° indicates the Warburg impedance, confirming the diffusion of ions into the pore of the electrode material and the formation of the electric double layer [58]. In contrast, HSC shows a significantly lower impedance window compared to the other two devices, indicating lower contact resistance between the electrode and electrolyte interfaces. Analysing the Bode plot (Fig. 4h), SSC and HSC exhibit phase shift responses that closely approximate the ideal capacitive phase shift of -90° . HSC demonstrates an increasing phase shift, having a maximum declination of -56.8° which is a contribution between the capacitive

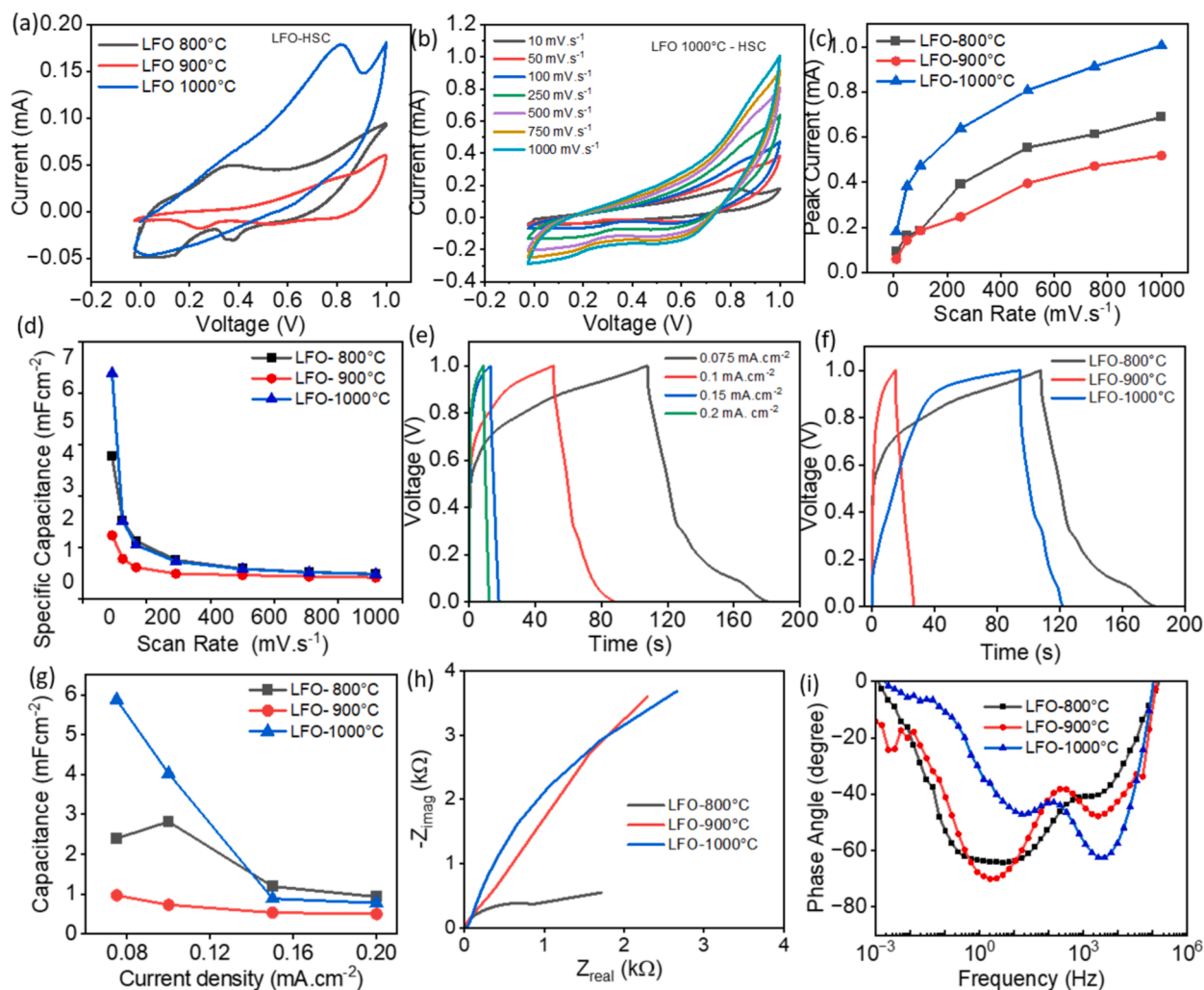


Fig. 5. (a) Comparison of CV curves of LFO-800 °C, LFO-900 °C, and LFO-1000 °C at a scan rate $10 \text{ mV}\cdot\text{s}^{-1}$ at 1 V (b) CV curves of LFO-1000 °C (c) Comparison of peak current of LFO-800 °C, LFO-900 °C, and LFO-1000 °C (d) Specific Capacitance from CV curve (e) GCD curves of LFO-1000 °C at different scan rates (f) Comparison of GCD curves of LFO-800 °C, LFO-900 °C, and LFO-1000 °C at $0.25 \text{ mA}\cdot\text{cm}^{-2}$ (g) Specific Capacitance from GCD curve (h) and (i) Nyquist and Bode plots of the devices.

and pseudocapacitive (faradaic) behaviours, and SSC has a declining phase shift having a maximum declination of -64.3° which is comparatively closer to capacitive behaviour. EIS analysis predicts that HSC exhibits high capacitance as compared to SSC, as shown in Fig. 4i.

Influence of sintering on electrochemical properties of LFO-HSC: As per the previous studies, it was found that compared with SSC, the HSC in which the cathode LaFeO_3 sintered at 800 °C and a screen-printed graphite anode were used, had better performances. The extended study investigates how the sintering temperature of the LaFeO_3 electrode (800 °C, 900 °C, and 1000 °C) affects the electrochemical performance. Fig. 5a shows the CV response of the HSCs fabricated using the electrodes LFO-800 °C, LFO-900 °C, and LFO-1000 °C at a scan rate of $10 \text{ mV}\cdot\text{s}^{-1}$ for 1 V. The specific capacitance values measured at this scan rate of LFO-800 °C show a specific capacitance of $3.93 \text{ mF}\cdot\text{cm}^{-2}$, LFO-900 °C has a specific capacitance of $1.47 \text{ mF}\cdot\text{cm}^{-2}$, and LFO-1000 °C exhibits a specific capacitance of $6.52 \text{ mF}\cdot\text{cm}^{-2}$. The curves have an almost quasi-rectangular shape, indicating a nearly mirror-image current response at higher scan rates. Notably, LFO-1000 °C-based HSC stands out with the highest peak current and the largest area under the CV curve, suggesting superior performance among the three devices. The variation of the CV curves with different scan rates for LFO-1000 °C HSC is given in Fig. 5b and similar for LFO-800 °C and LFO-900 °C are given in Fig. S9a and S9b. Examination of the peak current

reveals that LFO-1000 °C has a wider peak current window compared to the other two devices, as shown in Fig. 5c. The maximum peak current value of LFO-800 °C reaches a peak current of 0.689 mA, LFO-900 °C achieves a peak current of 0.518 mA, and LFO-1000 °C attains a peak current of 1 mA. LFO-1000 °C maintains relatively consistent peak current values across different scan rates, indicating its independence from scan rate variations. The specific capacitance values calculated from the CV curves further support this observation shown in Fig. 5d.

The GCD curves of the LFO-800 °C, LFO-900 °C, and LFO-1000 °C devices at different current densities are presented in Fig. S9c, S9d, and Fig. 5e respectively. To facilitate direct comparison, the GCD curves of LFO-800 °C, LFO-900 °C, and LFO-1000 °C at a current density of $0.25 \text{ mF}\cdot\text{cm}^{-2}$ reveal specific capacitance values of $2.39 \text{ mF}\cdot\text{cm}^{-2}$ for LFO-800 °C, $0.97 \text{ mF}\cdot\text{cm}^{-2}$ for LFO-900 °C, and $5.88 \text{ mF}\cdot\text{cm}^{-2}$ for LFO-1000 °C shown in Fig. 5f. The GCD curves for all three devices display a distorted linear triangular shape, indicative of their capacitive characteristics. The GCD curves of the LFO-900 °C device exhibit a higher voltage drop and poorer reversibility compared to the LFO-800 °C and LFO-1000 °C devices. This is reflected in the lower capacitive contribution of the LFO-900 °C device as shown in Fig. 5g. This lower performance is also confirmed in CV analysis, and it could be due to the surface morphology variation of the materials and could be found from the SEM analysis in Fig. 2. Each GCD cycle shows a small IR drop, which

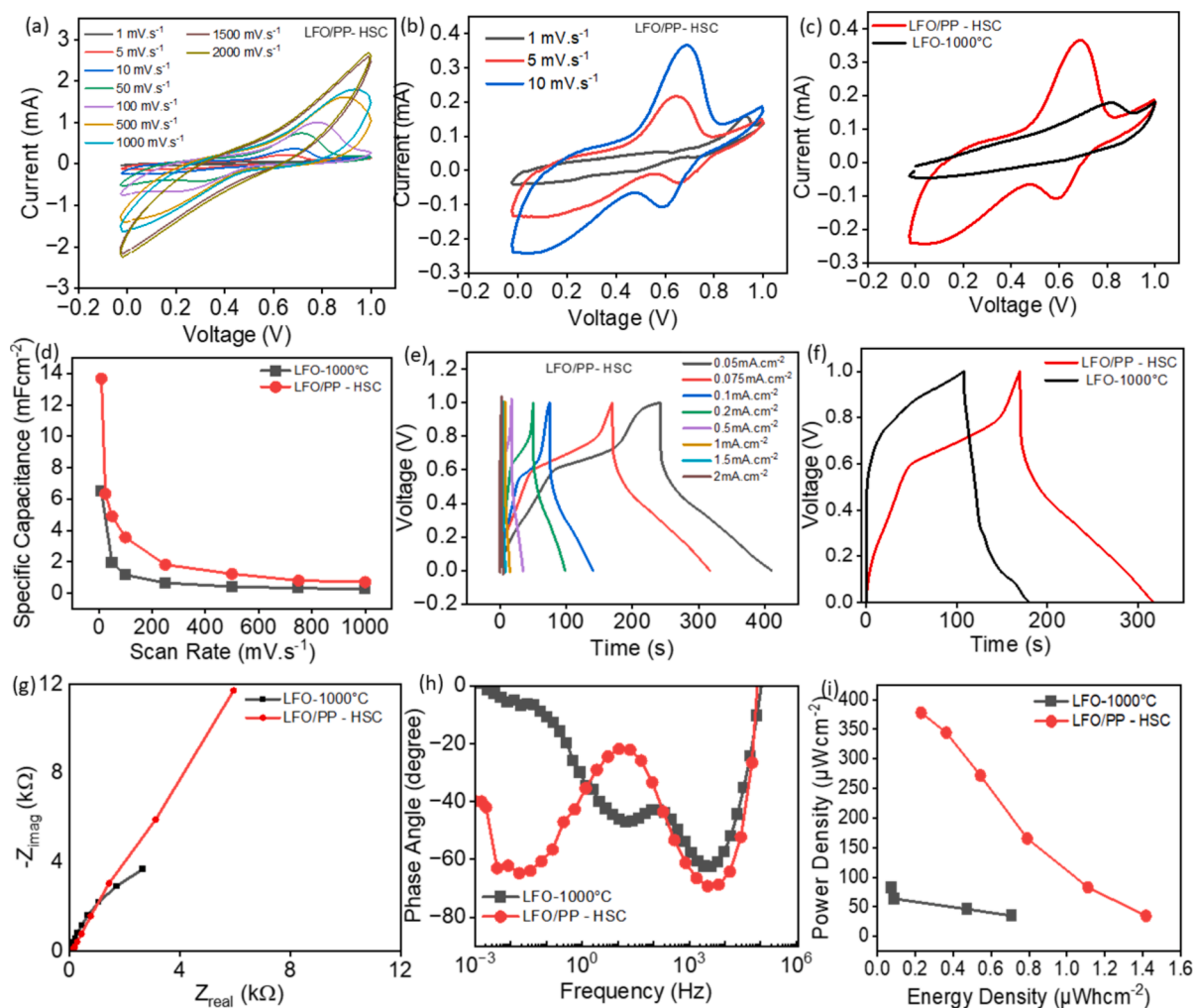


Fig. 6. CV curves of (a) LFO/PP-HSC (b) LFO/PP-HSC at lower scan rate (c) Comparison of CV curves of LFO/PP-HSC and LFO-1000 °C at 10 mV.s⁻¹ at 1 V (d) Specific Capacitance from CV curve (e) GCD curves of LFO/PP-HSC at different scan rates (f) Comparison of GCD curves of LFO/PP-HSC and LFO-1000 °C at 0.075 mA.cm⁻² (g) and (h) Nyquist and Bode plot for the HSCs (i) Ragone Plot of LFO/PP-HSC and LFO-1000 °C.

can be attributed to the contact resistance between the electrolyte and the active electrodes. The LFO-900 °C device demonstrates a faster discharging rate, with a large IR drop. Comparing the LFO-800 °C and LFO-1000 °C devices, the LFO-800 °C device exhibits a longer discharging time, as observed in the comparison graph (Fig. 5f). At lower current densities, the capacitance of the LFO-1000 °C device is dominant, while at higher current densities, the LFO-800 °C device exhibits a slightly higher capacitance. When considering the energy density and power density obtained from the GCD curves in Fig. S10, the LFO-1000 °C device demonstrates a higher power and energy density response compared to the other two devices. The highest energy densities for LFO-800 °C, LFO-900 °C, and LFO-1000 °C are 0.24 μWhcm⁻², 0.11 μWhcm⁻², and 0.71 μWhcm⁻², respectively. Regarding measured power density, for LFO-800 °C it is 31.91 μWcm⁻², for LFO-900 °C is 33.63 μWcm⁻², and for LFO-1000 °C is 34.95 μWcm⁻².

The EIS measurements were conducted in the frequency range of 1 mHz to 1 MHz, and the results are presented in Fig. 5h. Analysis of the Nyquist plot reveals that the LFO-1000 °C device exhibits a comparatively higher impedance window, indicating higher resistance in the system. In contrast, the LFO-900 °C device displays a relatively lower impedance at lower frequencies. Notably, the LFO-800 °C device demonstrates a significantly lower impedance window compared to the other two devices, suggesting a lower contact resistance between the electrode and the electrolyte. ESR obtained from the higher frequency region shows that LFO-800 °C has an ESR of 0.8 Ω, LFO-900 °C has an

ESR of 1 Ω, and LFO-1000 °C has an ESR of 0.1 Ω. The lower ESR of LFO-1000 °C indicates improved electrical conductivity and reduced resistive losses in the device. Examination of the Bode plot given in Fig. 5i shows that all three devices, LFO-800 °C, LFO-900 °C, and LFO-1000 °C, exhibit a good phase shift response, with the values relatively close to the ideal capacitive phase shift of -90°. Among the devices, LFO-800 °C and LFO-1000 °C demonstrate the highest phase angles, measuring -64° and -62°, respectively. This indicates a more balanced contribution between the capacitive and pseudocapacitive (faradaic) behaviours in these devices. In contrast, LFO-900 °C follows with a phase angle of -70°, suggesting a more dominant capacitive behaviour compared to the pseudocapacitive contribution. The lower impedance and higher phase angles observed in LFO-800 °C and LFO-1000 °C indicate improved electrode-electrolyte interactions and a more balanced utilization of the capacitive and pseudocapacitive charge storage mechanisms, which can contribute to enhanced energy storage and power delivery capabilities. Upon further analysis, it is observed that the performance parameters of the LFO-1000 °C device align more closely with the desired characteristics, exhibiting both higher energy density and power density, thereby striking a balanced overall performance. Hence, the electrochemical characteristics show that the performance order of LaFeO₃ HSC is observed as LFO 1000 °C > LFO 800 °C > LFO 900 °C. In addition to this, we also tested a new device that was fabricated using LaFeO₃ sintered at 1100 °C. After conducting an electrochemical analysis, it was concluded that the 1100 °C sintering temperature is less

favourable than the LFO-1000 sample, as demonstrated in Fig. S11 in the supporting information.

Influence of conductive polymer coating on the top of LFO: In the previous section, the LFO-1000 °C HSC exhibited superior performance. In this study, the LaFeO₃ 1000 °C electrode was surface-modified with conducting polymer PEDOT:PSS to improve energy storage capabilities. Fig. 6a shows the CV curve for LFO/PP-HSC by varying the scan rate from 1 to 2000 mV•s⁻¹ across a potential range of 0 to 1 V. The distinct peaks in the CV graph are more visible at lower scan rates (shown in Fig. 6b) compared to higher scan rates. At lower scan rates of 1–10 mV•s⁻¹, the CV graph shows clear anodic and cathodic redox peaks. This is because slower scan rates allow enough time for the electrochemical processes to reach equilibrium. This enables the clear separation and observation of the distinct redox peaks associated with the pseudocapacitive behaviour of the lanthanum ferrite. The lower scan rate provides ample time for the ions to move in and out of the electrode materials, allowing the redox reactions to be fully reflected in the CV curve. The graph has a distorted rectangular shape with these peaks, producing mirror-image current responses. The positive peak in the CV graph corresponds to the redox reactions occurring at the lanthanum ferrite with PEDOT: PSS cathode. The lanthanum ferrite component can undergo reversible redox reactions, where the metal ions change their oxidation states during charging and discharging [59]. The addition of PEDOT: PSS enhances the pseudocapacitive behaviour and improves the electrochemical performance of the cathode. The redox reactions at the cathode contribute to the pseudocapacitance, leading to the positive peak. The negative peak in the CV graph is associated with the EDL behaviour of the graphite anode. During charging, the graphite anode stores energy by forming an EDL, a non-faradaic process. Adding PEDOT: PSS to the lanthanum ferrite cathode further enhances the pseudocapacitive behaviour and improves the energy storage performance of the HSC. The PEDOT:PSS component provides additional redox-active sites and enhances the conductivity of the cathode material, leading to better charge storage and charge transfer kinetics. These two distinct peaks in the CV graph indicate the well-formed hybrid nature of the energy storage mechanism in the LFO/PP-HSC. Higher scan rates result in faster electrochemical processes, causing the redox peaks to become less distinct or even disappear. The pseudocapacitive contributions from the metal oxide cathode become more intertwined with the EDLC behaviour of the carbon anode. At higher scan rates, the ion diffusion kinetics within the electrode materials cannot keep up with the rapid changes in the applied potential, leading to a more capacitive-like response in the CV curve. The distinct redox peaks are suppressed, and the CV curve may exhibit a more rectangular shape, characteristic of an EDLC-dominated behaviour. This device's stable and high-performance characteristics are evident from the cyclic voltammogram, which shows a large area under the scan voltage range, suggesting relatively high specific capacitance and peak current. The CV curves of LFO-1000°C HSC and LFO/PP-HSC were compared at a scan rate of 10 mV•s⁻¹, shown in Fig. 6c. The analysis reveals that LFO-1000°C HSC exhibits no mirror-image currents, a small oxidation peak, and a relatively smaller polynomial area in the CV curve. In contrast, the PEDOT: PSS coated LFO displays a larger area under the polynomial curve, mirror-image current responses, and distinct oxidation and reduction peaks. This is reflected in the specific capacitance, where LFO/PP-HSC measures 13.68 mF•cm⁻², which is double that of LFO-1000 °C HSC, which has a specific capacitance of 6.52 mF•cm⁻². The maximum peak current values for LFO/PP-HSC (Fig. S12a) reach a peak of 1.79 mA, which is higher than the peak current of 1 mA observed for LFO-1000 °C HSC at a scan rate of 1000 mV•s⁻¹. These features are indicative of superior LFO/PP-HSC performance. The comparison of the peak currents (Fig. S12a) and specific capacitance (Fig. 6d) derived from the CV curve analysis demonstrates that the LFO/PP HSC exhibits a higher peak current response and specific capacitance.

Fig. 6e represents the GCD curves for LFO/PP-HSC in different current densities. The resulting GCD curves displayed a distorted linear

triangular shape, indicating the device has the capacitance characteristics of an HSC. The 0.05 mA current exhibited a higher discharge rate, suggesting faster charging and slower discharging. This implies the device has the potential to provide high energy density and power density. The formation of the charging and discharging curves is very similar to that of a battery-like GCD curve. Each GCD cycle showed an IR drop, which is attributed to the contact resistance between the electrolyte and the active electrodes. The comparison of the GCD response in Fig. 6f at a current of 0.075 mA•cm⁻² shows both the LFO-1000 °C HSC and LFO/PP-HSC materials exhibit a distorted triangular shape in their GCD curves, which is a common characteristic of HSC. However, the LFO/PP-HSC has a longer discharge duration compared to the LFO-1000 °C based HSC. This observation is evident in the specific capacitance values presented in Fig. S12b, derived from the GCD analysis. The LFO/PP-HSC demonstrates a higher specific capacitance of 12.01 mF•cm⁻², in contrast to LFO-1000 °C, which shows a specific capacitance of 5.87 mF•cm⁻² at a current density of 0.0075 mA•cm⁻². When evaluating the energy density and power density characteristics derived from the GCD curves, LFO-1000 °C displays a lower energy density 0.71 μWh•cm⁻² and power density 82.4 μW•cm⁻² compared to the LFO/PP-HSC which is 1.41 μWh•cm⁻² and 378 μW•cm⁻², respectively shown in Fig. 6i. The modification of the LFO-1000 °C material, likely through the incorporation of PEDOT:PSS, has addressed this semi-conductivity and enabled the LFO/PP-HSC to demonstrate a significantly higher energy density while maintaining relatively good power density performance.

The EIS analysis conducted in the frequency range of 1 mHz to 1 MHz revealed notable differences between the LFO-1000 °C HSC and LFO/PP-HSC. The Nyquist plot, Fig. 6g analysis shows that LFO-1000 °C HSC exhibits a significantly lower impedance window, indicating a lower contact resistance between the electrode and electrolyte. But, the LFO/PP-HSC material displays a larger impedance window, suggesting higher resistance in the system. However, the ESR obtained from the higher frequency region is found to be negligible for both LFO-1000 °C HSC and LFO/PP-HSC. Specifically, LFO-1000 °C has an ESR value of 0.11 Ω, while LFO/PP-HSC exhibits an ESR value of 0.207 Ω. These low ESR values indicate minimal resistance in the overall system, leading to lower energy losses and improved power delivery capabilities. These observed values are slightly varied with the values observed from the equivalent fitting circuit of the EIS data as shown in Fig. S13 and Table S1. The Bode plot analysis of the phase shift response in Fig. 6h reveals both LFO/PP-HSC and LFO-1000 °C HSC exhibit a sinusoidal wave-like behaviour, which can be attributed to the combination of EDLC and pseudocapacitive contribution. The phase angle first decreases due to the dominance of the capacitive behaviour, then increases due to the inductive behaviour, and finally decreases again as the capacitive behaviour becomes dominant at higher frequencies. Notably, the formation of the peak in the phase angle is slightly larger for LFO/PP-1000 °C compared to LFO-1000 °C which is 64.8° and 62.52° respectively, indicating that the inductive behaviour of LFO-1000 °C is not as strong. This suggests that the LFO/PP-HSC still exhibits a more desirable phase shift response, reflecting its enhanced capacitive behaviour and overall superior performance. This establishes the LFO/PP HSC as a superior performance compared to the LFO-1000°C HSC. The distinct differences observed in the electrochemical characteristics between the two materials suggest that the modifications made to the LFO-1000 have significantly improved its electrochemical performance and suitability for high-performance supercapacitor applications. Hence, due to the semiconductor properties, the electrochemical behaviour is significantly improved with the introduction of PEDOT: PSS as a coating in LFO, which enhances overall conductivity and stability, facilitates better electron transport and increases the active surface area available for ion interactions. Additionally, the PEDOT: PSS can participate in redox reactions, providing extra charge storage mechanisms while acting as a binder that maintains structural integrity during cycling. This combination results in faster charge/discharge rates, improved cycling stability, and a longer lifespan, making this HSC

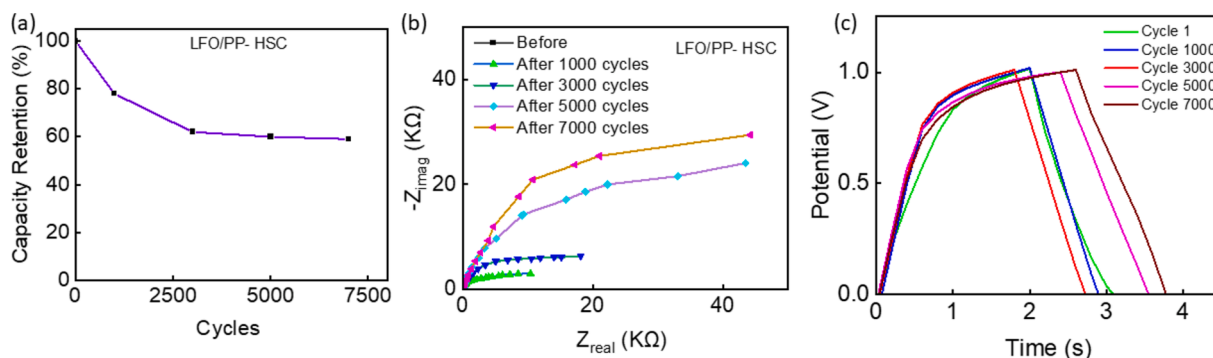


Fig. 7. Cyclic stability of the LFO/PP-HSC (a) Capacitive retention, (b) EIS variation in different cycles, and (c) GCD variation in different cycles.

configuration a promising advancement in energy storage technology. Further, to investigate the electrochemical and energy-storing performances of the HSCs, individual electrodes such as LFO/PP and graphite were investigated using 3-electrode measurement system and are discussed in supporting information along with Fig. S14.

Cyclic stability is one of the most crucial parameters that reflect energy storage device lifespan, which is expressed in terms of capacity retention (%). The cyclic stability of the LFO/PP-HSC in 6 M KOH electrolyte was examined by repeated GCD measurements over 7000 cycles with a voltage window of 0 to 1 V at a current density of $200 \mu\text{A}\cdot\text{cm}^{-2}$. The LFO/PP-HSC is showing around 60 % capacity retention after 7000 cycles, shown in Fig. 7a. The EIS growth is carried out at different points between cycles, as shown in Fig. 7b. The impedance's real and imaginary parts increase as cycling decreases due to electrode and electrolyte degradation. This increase in the impedance resulted in the reduction of the device capacity. The variation in the discharging curve at different cycles during long charging discharging is shown in Fig. 7c. To investigate the electrode surface variation and device performances during long charging and discharging, we measured 10,000 cycles for a new batch of HSCs, and the observed performances are given in Fig. S15. The observed first and last 10,000 GCD cycles are given in Fig. S15a and the observed capacitive retention are given in Fig. S15b. The LFO/PP-HSC shows around 67.8 % capacity retention after 10,000 cycles, as shown in Fig. S14b (we noticed some minor variations in retention for the sample prepared in different batches, which could be due to surface property changes). We observed notable changes in the electrode surface morphology before and after long charging-discharging. Fig. S15c represents the SEM image of the electrode before electrochemical characterisation. We observed that the material's surface properties varied after long charging-discharging. Small material clusters are formed which could be found in SEM images in Fig. S15d after the 10,000-cycle test due to electrode – electrolyte interaction.

4. Conclusion

In this work, we studied the energy-storing performances of LaFeO_3 perovskite for the next generation of energy storage. We investigated the electrochemical performances of LaFeO_3 with the fabrication of a symmetric supercapacitor (SSC) and hybrid supercapacitor (HSC). Here, for the HSC development, the LaFeO_3 acts as a cathode electrode, and graphite acts as an anode electrode. To analyze the energy storing performances, we sintered the LaFeO_3 at three different temperatures (800°C , 900°C , and 1000°C), which led to varying the bulk properties and also surface treated with a conductive polymer (Poly(3,4-ethylene dioxythiophene) polystyrene sulfonate (PEDOT: PSS)). Based on these electrodes, we developed two sets of HSCs and an SSC, which consist of set 1 with LaFeO_3 (LFO-SSC), set 2 with pristine LaFeO_3 (LFO-HSC), and set 3 based on the $\text{LaFeO}_3/\text{PEDOT:PSS}$ (LFO/PP-HSC). We observed that the LaFeO_3 sintered at 1000°C shows high performances, and the

densities for HSCs based on LFO- 800°C , LFO- 900°C , and LFO- 1000°C are $0.24 \mu\text{Wh}\cdot\text{cm}^{-2}$, $0.11 \mu\text{Wh}\cdot\text{cm}^{-2}$, and $0.71 \mu\text{Wh}\cdot\text{cm}^{-2}$, respectively. Further, with surface modification using the conducting polymer, the LFO/PP-HSC exhibits a higher specific capacitance of $12.01 \text{ mF}\cdot\text{cm}^{-2}$ compared to LFO- 1000°C , which has a specific capacitance of $5.87 \text{ mF}\cdot\text{cm}^{-2}$ at a current density of $0.0075 \text{ mA}\cdot\text{cm}^{-2}$. When evaluating the energy density and power density characteristics derived from the GCD curves, LFO- 1000°C displays a lower energy density of $0.71 \mu\text{Wh}\cdot\text{cm}^{-2}$ and power density of $82.4 \mu\text{W}\cdot\text{cm}^{-2}$ compared to the LFO/PP-HSC, which is $1.41 \mu\text{Wh}\cdot\text{cm}^{-2}$ and $378 \mu\text{W}\cdot\text{cm}^{-2}$ respectively. These findings contribute significantly to the development of more efficient and effective energy storage technologies using perovskite materials. The studies reveal that the ABO_3 perovskite demonstrates exceptional electrochemical properties, including high specific capacitance and excellent rate capability, attributed to its distinctive structure, inherent redox activity, and rapid ion diffusion properties.

CRedit authorship contribution statement

Reshma Nair: Writing – review & editing, Writing – original draft, Visualization, Validation, Methodology, Investigation, Formal analysis. **Kiranmai Uppuluri:** Writing – original draft, Methodology, Investigation, Formal analysis. **Febin Paul:** Writing – original draft, Visualization, Methodology, Investigation, Formal analysis. **Keith Sirengo:** Methodology, Investigation. **Dorota Swagierczak:** Writing – review & editing, Writing – original draft, Validation, Project administration, Methodology, Investigation, Formal analysis. **Suresh C Pillai:** Writing – review & editing, Writing – original draft, Methodology, Investigation, Funding acquisition, Formal analysis. **Libu Manjakkal:** Writing – review & editing, Writing – original draft, Visualization, Supervision, Resources, Project administration, Methodology, Investigation, Funding acquisition, Formal analysis, Data curation, Conceptualization.

Declaration of competing interest

The authors declare that they have no known competing financial interests or personal relationships that could have appeared to influence the work reported in this paper.

Acknowledgements

This work is supported by the Edinburgh Napier University SCEBE Starter Grant (N480-000) and LM acknowledged The Carnegie Trust for the Universities of Scotland Grant (R2552-00). This work was partly supported by Science Foundation Ireland (SFI-20/EPSC/3710) and also by the UK Engineering and Physical Sciences Research Council (EPSRC) through grant Ref. EP/V003380/1 ('Next Generation Energy Autonomous Textile Fabrics based on Triboelectric Nanogenerators'). This work also supported by National Science Centre (Poland) through the TESLA (CHIST-ERA IV -857925) project.

Appendix A. Supplementary data

Supplementary data to this article can be found online at <https://doi.org/10.1016/j.cej.2024.158781>.

Data availability

Data will be made available on request.

References

- P. Sivakumar, C.J. Raj, R. R. L. Kulandaivel, J. Park, H. Jung, Influence of heat-treatment temperature on the improvement of the electrochemical performance of CoMoO₄ nanomaterials for hybrid supercapacitor application, *Ceramics Inter.* 48 (19, Part B) (2022) 29018–29024.
- Z. Jia, C. Cheng, X. Chen, L. Liu, R. Ding, J. Ye, J. Wang, L. Fu, Y. Cheng, Y. Wu, Applications of all-inorganic perovskites for energy storage, *Mater. Adv.* 4 (1) (2023) 79–104.
- G.R. Monama, K.E. Ramohlola, E.I. Iwuoha, K.D. Modibane, Progress on perovskite materials for energy application, *Results in Chem.* 4 (2022) 100321.
- Y. Baba, I. Shimoyama, N. Hirao, T. Izumi, Interaction between Ultra-Trace Amount of Cesium and Oxides Studied by Total-Reflection X-Ray Photoelectron Spectroscopy, *e-J. Surf. Sci. Nanotechnol.* 13 (2015) 417.
- A. Muzaffar, M.B. Ahamed, K. Deshmukh, J. Thirumalai, A review on recent advances in hybrid supercapacitors: Design, fabrication and applications, *Renew. Sustain. Energy Rev.* 101 (C) (2019) 123–145.
- K. Poonam, A. Sharma, S.K. Arora, Tripathi, Review of supercapacitors: Materials and devices, *J. Energy Storage* 21 (2019) 801–825.
- G. Wang, L. Zhang, J. Zhang, A review of electrode materials for electrochemical supercapacitors, *Chem. Soc. Rev.* 41 (2) (2012) 797–828.
- F. Wang, X. Wu, X. Yuan, Z. Liu, Y. Zhang, L. Fu, Y. Zhu, Q. Zhou, Y. Wu, W. Huang, Latest advances in supercapacitors: from new electrode materials to novel device designs, *Chem. Soc. Rev.* 46 (22) (2017) 6816–6854.
- P. Goel, S. Sundriyal, V. Shrivastav, S. Mishra, D.P. Dubal, K.-H. Kim, A. Deep, Perovskite materials as superior and powerful platforms for energy conversion and storage applications, *Nano Energy* 80 (2021) 105552.
- L. Zhu, R. Ran, M. Tadé, W. Wang, Z. Shao, Perovskite materials in energy storage and conversion, *Asia-Pacific J. Chem. Eng.* 11 (3) (2016) 338–369.
- D. Meng, H. Gu, Q. Lu, Y. Zhao, G. Zhu, Y. Zhang, Q. Zhong, Y. Bu, Advances and Perspectives for the Application of Perovskite Oxides in Supercapacitors, *Energy & Fuels* 35 (21) (2021) 17353–17371.
- O. Guillon, Ceramic materials for energy conversion and storage: A perspective, *International J. Ceramic Eng. Sci.* 3 (3) (2021) 100–104.
- M. Hussain, M.M. Alanazi, S.A. Abdelmohsen, S.D. Alahmari, M. Abdullah, S. Aman, A. Dahshan, A. Henaish, Z. Ahmad, H.M.T. Farid, Hydrothermal synthesis of Nd-doped FeTiO₃ perovskite electrode for enhanced energy storage applications, *J. Energy Storage* 84 (2024) 110920.
- A. Khan, M. Orbay, N. Dupré, E. Gautron, E.L. Calvez, O. Crosnier, A. Balducci, T. Brousse, Lithium storage behaviour of AgNbO₃ perovskite: Understanding electrochemical activation and charge storage mechanisms, *Energy Storage Mater.* 70 (2024) 103431.
- A. Rai, A.L. Sharma, A.K. Thakur, Evaluation of aluminium doped lanthanum ferrite based electrodes for supercapacitor design, *Solid State Ionics* 262 (2014) 230–233.
- P.M. Shafi, V. Ganesh, A.C. Bose, LaMnO₃/RGO/PANI Ternary Nanocomposites for Supercapacitor Electrode Application and Their Outstanding Performance in All-Solid-State Asymmetrical Device Design, *ACS Appl. Energy Mater.* 1 (6) (2018) 2802–2812.
- T. Kang, P. Nakhanev, K.J. Wang, Y. Chen, Y.G. Chung, H.S. Park, Anion storing, oxygen vacancy incorporated perovskite oxide composites for high-performance aqueous dual ion hybrid supercapacitors, *J. Energy Chem.* 94 (2024) 646–655.
- H.S. Magar, A. Mansour, A.B.A. Hammad, Advancing energy storage and supercapacitor applications through the development of Li⁺-doped MgTiO₃ perovskite nano-ceramics, *Sci. Rep.* 14 (1) (2024) 1849.
- P.M. Shafi, D. Mohapatra, V.P. Reddy, G. Dhakal, D.R. Kumar, D. Tuma, T. Brousse, J.-J. Shim, Sr- and Fe-substituted LaMnO₃ Perovskite: Fundamental insight and possible use in asymmetric hybrid supercapacitor, *Energy Storage Mater.* 45 (2022) 119–129.
- J. Li, W. Luo, X. Wang, C. Yu, Y. Zhang, F. Meng, Preparation and research of high-performance LaFeO₃/RGO supercapacitor, *Journal of Solid State, Electrochem.* 26 (2022) 1291–1301.
- E. Harputlu, C. Geçgel, Fabrication of LaFeO₃/g-C₃N₄@reduced graphene oxide 3-dimensional nanostructure supercapacitor, *Journal of Materials Science: Mater. Electron.* 33 (2022) 1–17.
- N. Sivakumar, P. Nagaraju, A. Alsalmé, A. Alghamdi, R. Jayavel, Enhanced electrochemical performance of lanthanum ferrite decorated reduced graphene oxide nanocomposite electrodes prepared by in situ microwave irradiation for energy storage applications, *Int. J. Energy Research* 45 (4) (2021) 5272–5282.
- C.A.L. Dixon, C.M. Kavanagh, K.S. Knight, W. Kockelmann, F.D. Morrison, P. Lightfoot, Thermal evolution of the crystal structure of the orthorhombic perovskite LaFeO₃, *J. Solid State Chem.* 230 (2015) 337–342.
- F.H. Taylor, J. Buckeridge, C.R.A. Catlow, Defects and Oxide Ion Migration in the Solid Oxide Fuel Cell Cathode Material LaFeO₃, *Chem. Mater.* 28 (22) (2016) 8210–8220.
- B.T. Flynn, K.H.L. Zhang, V. Shutthanandan, T. Varga, R.J. Colby, R.P. Oleksak, S. Manandhar, M.H. Engelhard, S.A. Chambers, M.A. Henderson, G.S. Herman, S. Thevuthasan, Growth and surface modification of LaFeO₃ thin films induced by reductive annealing, *Appl. Surf. Sci.* 330 (2015) 309–315.
- M. Papac, V. Stevanović, A. Zakutayev, R. O'Hayre, Triple ionic–electronic conducting oxides for next-generation electrochemical devices, *Nature Materials* 20 (3) (2021) 301–313.
- Z. Zhu, H. Peelaers, C.G. Van de Walle, Electronic and protonic conduction in LaFeO₃, *J. Mater. Chem. A* 5 (29) (2017) 15367–15379.
- F.H. Taylor, LaFeO₃ as a base material for cathode applications in intermediate temperature solid oxide fuel cells, UCL (University College London), 2019.
- P. Sivakumar, C.J. Raj, A.D. Savariraj, R. Manikandan, K. Karuppasamy, A. Alfantazi, H. Jung, The Interwoven Structured Two-Dimensional NiCo Layered Double Hydroxide Tortuous Nanosheet as Performance-Enhanced Electrode Material toward Battery-Type Supercapacitor, *Int. J. Energy Res.* 2024 (1) (2024) 3149906.
- M. Kumar, P. Sinha, T. Pal, K.K. Kar, Materials for supercapacitors, Performance, Handbook of Nanocomposite Supercapacitor Materials II, 2020, pp. 29–70.
- E. Harputlu, C. Geçgel, Fabrication of LaFeO₃/g-C₃N₄@reduced graphene oxide 3-dimensional nanostructure supercapacitor, *J. Mater. Sci. Mater. Electron.* 33 (34) (2022) 25687–25703.
- Y. Shao, M.F. El-Kady, J. Sun, Y. Li, Q. Zhang, M. Zhu, H. Wang, B. Dunn, R. B. Kaner, Design and Mechanisms of Asymmetric Supercapacitors, *Chem. Rev.* 118 (18) (2018) 9233–9280.
- K. Kumar, A.K. Sebastian, P.R. Markapudi, M. Beg, S. Sundaram, A. Hussain, L. Manjakkal, Opto-electrochemical variation with gel polymer electrolytes in transparent electrochemical capacitors for iontronics, *Appl. Phys. Lett.* 124 (2024) 111603.
- P. Nandakumar, A. Sankar, A. Ganesh, A. Ba, D. r., Electrochemical Performance of Carbon Materials, *Oriental J. Chem.* 38 (2022) 604–609.
- B. Pal, S. Yang, S. Ramesh, V. Thangadurai, R. Jose, Electrolyte selection for supercapacitive devices: a critical review, *Nanoscale Adv.* 1 (10) (2019) 3807–3835.
- B. Karamanova, A. Stoyanova, M. Shipochka, S. Veleva, R. Stoyanova, Effect of Alkaline-Basic Electrolytes on the Capacitance Performance of Biomass-Derived Carbonaceous Materials, *Materials* 13 (13) (2020).
- U. Rednam, P.E. Lokhande, R. Aepuru, A. Thirumurugan, A. Akbari-Fakhrbadi, S. K. Kamaraj, Evaluation of structural and electrochemical properties of LaFeO₃-8Cu_{0.2-x}Ti_xO (x=0.1) perovskite oxide, *Mater. Chem. Phys.* 328 (2024) 130014.
- L. Manjakkal, C.G. Núñez, W. Dang, R. Dahiya, Flexible self-charging supercapacitor based on graphene-Ag-3D graphene foam electrodes, *Nano Energy* 51 (2018) 604–612.
- A.R. Peringath, M.A.H. Bayan, M. Beg, A. Jain, F. Pierini, N. Gadegaard, R. Hogg, L. Manjakkal, Chemical synthesis of polyaniline and polythiophene electrodes with excellent performance in supercapacitors, *J. Energy Storage* 73 (2023) 108811.
- A.C.S. Chandran, J. Schneider, N. Nair, B. Bill, N. Gadegaard, R. Hogg, S. Kumar, L. Manjakkal, Enhancing Supercapacitor Electrochemical Performance with 3D Printed Cellular PEEK/MWCNT Electrodes Coated with PEDOT: PSS, *ACS Omega* 9 (31) (2024) 33998–34007.
- M. Beg, K.M. Alcock, A. Titus Mavelil, D. O'Rourke, D. Sun, K. Goh, L. Manjakkal, H. Yu, Paper Supercapacitor Developed Using a Manganese Dioxide/Carbon Black Composite and a Water Hyacinth Cellulose Nanofiber-Based Bilayer Separator, *ACS Appl. Mater. Interf.* 15 (44) (2023) 51100–51109.
- R.K. Bordia, S.-J.-L. Kang, E.A. Olefsky, Current understanding and future research directions at the onset of the next century of sintering science and technology, *J. American Ceramic Soc.* 100 (6) (2017) 2314–2352.
- M.M. Vadiyar, S.C. Bhise, S.K. Patil, S.S. Kolekar, A.R. Shelke, N.G. Deshpande, J.-Y. Chang, K.S. Ghule, A.V. Ghule, Contact angle measurements: a preliminary diagnostic tool for evaluating the performance of ZnFe₂O₄ nano-flake based supercapacitors, *Chem. Commun.* 52 (12) (2016) 2557–2560.
- M. Kaewpanha, T. Suriwong, W. Wamae, P. Nunocha, Synthesis and Characterization of Sr-doped LaFeO₃ perovskite by sol-gel auto-combustion method, *J. Physics: Conference Series* 1259 (2019) 012017.
- M.T. Kay Thi Tun, NweNweAung, Structural, Optical and Electrical Properties of LaFeO₃ LACOO₃ and LaFeO₃ Nano Crystalline Powders, Myanmar Academy of Arts and Science (MAAS) (2019).
- A. Nadarajan, G.-T. Pan, T.-C.-K. Yang, The exploration of Lanthanum based perovskites and their complementary electrolytes for the supercapacitor applications, *Results in Physics* 7 (2017).
- N. Sharma, H.S. Kushwaha, S.K. Sharma, K. Sachdev, Fabrication of LaFeO₃ and rGO-LaFeO₃ microspheres based gas sensors for detection of NO₂ and CO, *RSC Adv.* 10 (3) (2020) 1297–1308.
- V. Thiruvankadam, R. Sivasubramanian, S. Hussain, A. Ashok, A Facile Synthesis of Neurotransmitters, *ChemistrySelect* 2 (2017) 5570–5577.
- Q. Zhao, R. Jamal, L. Zhang, M. Wang, T. Abdiryim, The structure and properties of PEDOT synthesized by template-free solution method, *Nanoscale Res Lett* 9 (1) (2014) 557.
- M.R. Kumar, M.S. Freund, Electrically conducting collagen and collagen–mineral composites for current stimulation, *RSC Advances* 5 (71) (2015) 57318–57327.
- E. Susanti, P. Wulandari, Herman, Effect of localized surface plasmon resonance from incorporated gold nanoparticles in PEDOT:PSS hole transport layer for hybrid

- solar cell applications, *Journal of Physics: Conference Series* 1080 (1) (2018) 012010.
- [52] Y. Jiang, J. Liu, Definitions of Pseudocapacitive Materials: A Brief Review, *ENERGY & Environ. Mater.* 2(1) (2019) 30-37.
- [53] Y. Gogotsi, R.M. Penner, Energy Storage in Nanomaterials – Capacitive, Pseudocapacitive, or Battery-like? *ACS Nano* 12 (3) (2018) 2081–2083.
- [54] W.-Y. Lee, H.J. Yun, J.-W. Yoon, Characterization and magnetic properties of LaFeO₃ nanofibers synthesized by electrospinning, *J. Alloy. Compound.* 583 (2014) 320–324.
- [55] G. Nandikes, P. Pathak, M. Karthikeyan, A.A.M. Abahussain, L. Singh, Mesoporous LaFeO₃ perovskite as an efficient and cost-effective oxygen reduction reaction catalyst in an air cathode microbial fuel cell, *Int. J. Hydrogen Energy* 52 (2024) 627–641.
- [56] W. Zhou, Z. Liu, W. Chen, X. Sun, M. Luo, X. Zhang, C. Li, Y. An, S. Song, K. Wang, X. Zhang, A Review on Thermal Behaviors and Thermal Management Systems for Supercapacitors, *Batteries* 9 (2) (2023) 128.
- [57] S. Zhang, N. Pan, Supercapacitors Performance Evaluation, *Adv. Energy Mater.* 5 (6) (2015) 1401401.
- [58] A.C. Lazanas, M.I. Prodromidis, Electrochemical Impedance Spectroscopy—A Tutorial, *ACS Measurement Science Au* 3 (3) (2023) 162–193.
- [59] X. Zhang, C. Fu, D. Luo, X. Liu, Q. Wang, B. Li, G. Li, L. Li, Chemical bonding of perovskite LaFeO₃ with Li_{1.2}Mn_{0.6}Ni_{0.2}O₂ to moderate anion redox for achieving high cycling stability, *J. Energy Chem.* 79 (2023) 330–339.